Trapped CO$_2$ in Carbon Nanotube Bundles

Christopher Matranga,*,† Liang Chen,†,‡ Milton Smith,† Edward Bittner,†
J. Karl Johnson,†,‡ and Bradley Bockrath†

National Energy Technology Laboratory, United States Department of Energy, P.O. Box 10940,
Pittsburgh, Pennsylvania 15236 and Department of Chemical and Petroleum Engineering, University of
Pittsburgh, Pittsburgh, Pennsylvania 15261

Received: August 19, 2003; In Final Form: September 24, 2003

An infrared spectroscopic study of CO$_2$ that becomes permanently trapped in carbon nanotube bundles during thermolysis is reported. The temperature dependence of the ν_3 modes for trapped CO$_2$ is studied with two-dimensional infrared correlation spectroscopy. Computer simulations are used to extract the basic physics of trapped CO$_2$ and to make qualitative connections with changes seen in the infrared spectra. Experimental and simulated CO$_2$ adsorption studies point to a sequential filling of adsorption sites in opened nanotubes with interstitial sites preceding endohedral sites. The limited number of sites available to the trapped CO$_2$ species is used to facilitate a tentative assignment of vibrational peaks to specific sites in the nanotube bundles.

Introduction

During a study of the adsorption of gases on carbon nanotube samples, we have discovered that physically entrapped carbon dioxide is produced by a mild thermolysis of partially oxidized samples. Physical entrapment of gas molecules within bundles of single-walled carbon nanotubes (SWNTs) offers new opportunities to study molecules confined in a quasi one-dimensional system. The study of confined molecules is a particularly active area of research and carbon nanotubes serve as an experimental realization of a one-dimensional system. It is the unique structure of these SWNT bundles which is believed to create many novel adsorption and transport properties.[1−16]

Infrared spectroscopy is particularly well suited to study adsorption and confinement in carbon nanotube bundles. In addition to directly monitoring chemical functionalities on the material,[16−19] infrared spectroscopy has successfully probed adsorbate molecules for carbon nanotubes,[20−22] C$_{60}$,[23−28] and other types of carbon materials.[29] In the SWNT bundles, infrared studies have shown that oxygen-related functionalities block access to the interior of the nanotube and vacuum heating results in a decomposition of these functionalities, which opens access to the interior of the nanotubes.[17,20,21,30,31] Certain oxidative treatments have also been successful in opening access ports to interior sites in nanotubes.[20,21] Infrared studies of these opened nanotubes detected gas molecules adsorbed within the interior of the nanotubes.[20,21] At low pressures, adsorption of light gases in opened nanotubes only occurs at cryogenic temperatures and the open access ports mean that desorption occurs upon heating in a vacuum. Thus, these systems can only be studied over a fairly limited temperature range.

In this work, we present infrared spectroscopic studies of CO$_2$ that becomes permanently trapped in carbon nanotube bundles during the partial decomposition of oxygen-related functionalities on these bundles. Also, we use computer simulations to understand the behavior of the trapped CO$_2$ species and to understand how gas-phase CO$_2$ adsorbs in opened and closed nanotube bundles. We have observed trapped CO$_2$ in samples for periods of up to 2 months and over the temperature range (in a vacuum) of 5−700 K. Furthermore, after venting the nanotube samples to room air the trapped CO$_2$ remains within the nanotube bundles. We use the term permanent to describe the nature of the trapped CO$_2$ because of the extremely wide range of temperatures, time, and atmospheres we have observed this species for. We do expect that it is possible to ultimately release this trapped CO$_2$ with high-temperature annealing or a chemical release. Also, since oxygen-containing functionalities are responsible for creating this trapped CO$_2$, samples with a lower degree of functionality may not be capable of generating this species.

Experimental Methods

Infrared studies were performed in a stainless steel vacuum chamber equipped with a 70 L/s turbomolecular pump, roughing pump, precision leak valve, and differentially pumped optical windows (KBr). Pressure was measured with an ionization gauge. The system base pressure was in the low 10^{-8} Torr range after a 24-h pump down. The sample was manipulated inside the chamber with an XYZ translation stage and a rotation stage. Sample cooling and heating (∼5−700 K) was done with a liquid He/N$_2$ cryostat (ST-400 Model, Janis Research) equipped with a copper sample holder accommodating a blank and one sample.

The SWNT sample was purchased from Tubes@Rice as a "Purified Grade" suspended in toluene. This sample was produced by the laser ablation technique followed by a HNO$_3$/H$_2$SO$_4$ oxidative/purification treatment to remove amorphous and unwanted carbons.[32] The sample was dispersed directly on a 1-mm thick by 12.70-mm diameter plane parallel CaF$_2$ window (Janos Technology) and the solvent evaporated in a 120 °C oven for ∼5 min before being placed on the sample holder and transferred to vacuum. The blank was a separate plane parallel CaF$_2$ window placed on the same sample holder.

Infrared measurements were done with a Nicolet Nexus 670 ESP Fourier transform infrared spectrometer equipped with a liquid N$_2$ cooled narrow band MCT detector. All measurements

Trapped CO$_2$ in Carbon Nanotube Bundles

J. Phys. Chem. B, Vol. 107, No. 47, 2003 **12931**

were taken in the transmission geometry. Spectra are averaged over 1000 scans at 4 cm^{-1} resolution unless otherwise noted. Infrared scans were done by heating/cooling the sample to the desired temperature and allowing for complete thermal equilibrium ($\sim$20−30 min). A reference spectrum was then taken of the blank CaF$_2$ window followed by a spectrum of the nanotubes dispersed on the other CaF$_2$ window. This process was repeated at each temperature. Under these conditions, the samples were thermally stable and spectra taken at a given temperature did not change even over the course of hours.

Two-dimensional infrared correlation spectroscopy (2D IR) was used to analyze the temperature dependence of the infrared spectra. In 2D IR, infrared spectra are taken as a function of an external perturbation (e.g., temperature, pressure, time). The technique allows one to easily visualize coupled intensity variations because of this perturbation which occurs between highly convoluted spectral peaks. The correlation spectrum can be expressed as[33−35]

$$X(\nu_1, \nu_2) = \langle \tilde{\mathbf{y}}(\nu_1, T) \cdot \tilde{\mathbf{y}}(\nu_2, T') \rangle \quad (1)$$

$X(\nu_1, \nu_2)$ is a complex number, $X(\nu_1, \nu_2) = \Phi(\nu_1, \nu_2) + i\Psi(\nu_1, \nu_2)$, comprising two orthogonal components known as the synchronous, $\Phi(\nu_1, \nu_2)$, and asynchronous, $\Psi(\nu_1, \nu_2)$, 2D correlation intensities. The synchronous 2D correlation intensity represents simultaneous intensity variations measured at ν_1 and ν_2 which occur because of the external perturbation. The asynchronous 2D correlation intensity represents sequential intensity changes at ν_1 and ν_2.

The 2D IR method used here is described for the discrete case by Noda.[34,35] A set of dynamic spectra, $y_j(\nu) = y(\nu, T_j)$, are generated by subtracting from each individual spectrum a reference that corresponds to the averaged spectrum over all the temperatures. The dynamic spectra can be conveniently represented as a column vector:[34]

$$\tilde{\mathbf{y}}(\nu) = \begin{bmatrix} \tilde{\mathbf{y}}(\nu, T_1) \\ \tilde{\mathbf{y}}(\nu, T_2) \\ ... \\ \tilde{\mathbf{y}}(\nu, T_n) \end{bmatrix} \quad (2)$$

The synchronous spectrum is then given by the inner product of two dynamic spectrum vectors:[34]

$$\Phi(\nu_1, \nu_2) = \frac{1}{n-1} \tilde{y}(\nu_1)^T \tilde{y}(\nu_2) \quad (3)$$

The asynchronous spectrum is given by[34]

$$\Psi(\nu_1, \nu_2) = \frac{1}{n-1} \tilde{y}(\nu_1)^T \mathbf{N} \tilde{y}(\nu_2) \quad (4)$$

where $\mathbf{N}$ is the Hilbert transformation matrix:[34]

$$\mathbf{N} = \frac{1}{\pi} \begin{bmatrix} 0 & 1 & \frac{1}{2} & \frac{1}{3} & ... \\ -1 & 0 & 1 & \frac{1}{2} & ... \\ -\frac{1}{2} & -1 & 0 & 1 & ... \\ -\frac{1}{3} & -\frac{1}{2} & -1 & 0 & ... \\ ... & ... & ... & ... & ... \end{bmatrix} \quad (5)$$

2D correlation analysis is simplified when spectra are collected at evenly spaced increments along the external

TABLE 1: Lennard-Jones Potential Parameters for CO$_2$ and for the Carbons in Nanotubes

atom	σ(Å)	ϵ/k (K)
C	2.785	28.999
O	3.064	82.997
C (nanotube)	3.4	28.0

perturbation variable. For this reason, the spectra used for 2D analysis in this study were collected every 50 K from 50 to 550 K. At temperatures above 550 K, the intensity of the band analyzed with 2D IR becomes weak and difficult to detect. Spectra reported at other temperatures (5, 77, and 700 K) are included to show the temperature range over which we observe the reported phenomena. Synchronous and asynchronous spectra were calculated as described above using eqs 2−5.

Raman spectra were taken with a Nicolet Almega Dispersive Raman System with a 532-nm excitation source. The 10× objective of the microscopy attachment was used to collect spectra of samples dispersed on a CaF$_2$ window. A 1-s acquisition time added over 30 acquisitions was used for each spectrum. Estimated resolution is 1.5−2.5 cm^{-1} over the spectral range of 100−4000 cm^{-1}.

Simulation Methods

We have modeled two different scenarios in our simulations. In the first case, we model CO$_2$ molecules that are trapped inside the interior of individual nanotubes and in the interstitial regions of SWNT bundles. In this scenario, the number of molecules in the simulation is fixed (canonical, or *NVT* ensemble). In the second case, we consider an open system where CO$_2$ is allowed to adsorb onto the external and internal surfaces of SWNT bundles from the bulk gas phase. The number of molecules in the adsorption simulations fluctuates (grand canonical or μVT ensemble). The first scenario is meant to model the experiments involving trapped CO$_2$, whereas the μVT simulations mimic CO$_2$ dosing experiments. Canonical ensemble simulations were carried out by first performing grand canonical Monte Carlo (GCMC) simulations[36] to achieve a desired fixed coverage, after which the system was allowed to equilibrate and data were taken in the *NVT* ensemble. The GCMC algorithm consists of three types of moves, namely, translation and rotation of a single molecule, creation of a new molecule, and deletion of an existing molecule. Moves were attempted randomly with probability 20% for translation/rotation and 40% each for creation and deletion. The *NVT* simulations consist of translation/rotation moves only. Simulations were typically equilibrated for 10^7 moves, followed by data taking for 5 × 10^6 moves. The maximum displacement step size was adjusted during equilibration to achieve approximately a 40% acceptance ratio for combined translation and rotation moves. The CO$_2$–CO$_2$ interaction was described by the Harris−Yung potential model,[37] which employs three Lennard-Jones (LJ) sites and charges centered at each atom. The sites were held rigid (no bond vibration or bending allowed). Lorentz−Berthelot combining rules were used for the cross interactions. The LJ potential parameters are given in Table 1 where σ is the atomic diameter in Å and ϵ is the potential well depth such that ϵ/k is in units of k, where k is the Boltzmann constant. The charge on the carbon atom is $q_c = +0.6645e$ with the charge on the oxygen given by $q_O = -q_c/2$. The C−O bond length is 1.161 Å. The interaction potential between CO$_2$ and the nanotubes was taken as cross interactions between the LJ atoms of CO$_2$ and the C atoms of a graphene sheet, wrapped into a carbon nanotube. The graphite LJ parameters from Steele[38] were used for these calculations, with parameters shown

12932 *J. Phys. Chem. B, Vol. 107, No. 47, 2003*

Matranga et al.

TABLE 2: Classes of Nanotube Bundles Studied in the Molecular Simulations in This Work

bundle	number of (8,8) tubes	number of (9,9) tubes	number of (10,10) tubes	number of (11,11) tubes	number of (12,12) tubes	average diameter (Å)
1	2	2	10	2	2	13.56
2	4	10	2	2	0	12.35
3	0	0	9	0	0	13.56

in Table 1. The use of classical potentials to model the nanotube–fluid interactions precludes the modeling of electronic effects, such as the differences between metallic and nonmetallic nanotubes. However, this type of potential is accurate for modeling the adsorption of simple fluids, such as methane, adsorbed in bundles of carbon nanotubes.[39] The solid–fluid potential used in the simulation was smoothed by integrating over the positions of all the carbon atoms in the nanotube. The resulting integrated potential is solely a function of the distance r from the center of the nanotube. The smoothed potential was fitted to separate polynomials for endohedral (internal) and exohedral (external) adsorption for each LJ atom type (i.e., different polynomial coefficients for carbon–carbon and for oxygen–carbon interactions).

Three different nanotube bundles were considered in this work. Two bundles were constructed by randomly placing nanotubes of various diameters in a box and then optimizing the spacing between the nanotubes[40] to mimic the vacuum-heated sample. Each of these two bundles contained 18 nanotubes. The numbers of each type of nanotube in each bundle are given in Table 2. Bundles 1 and 2 are representative of heterogeneous bundles, that is, bundles with a heterogeneous distribution of nanotube diameters. Bundle 3 is a homogeneous bundle containing 9 (10,10) nanotubes packed into a perfect 3×3 array. This bundle is used to mimic the untreated nanotube samples because we only allow adsorption on the external surface (including grooves) of the bundle. The untreated tubes contain functionalities that block adsorption at interstitial and endohedral sites, therefore, considering only external/groove sites should be a valid approximation. We use a homogeneous bundle as a model for an unopened nanotubes bundle because previous work has shown that adsorption of gases on the external surface of homogeneous and heterogeneous bundles is virtually identical.[41] Periodic boundary conditions were applied in all three directions. The x and y dimensions of the simulation cell were large enough to eliminate nearest-neighbor interactions between periodic images to mimic isolated SWNT bundles.

Results and Discussion

Decomposition of Oxygen Functionalities and CO_2 Entrapment. Infrared spectra of the carbon nanotube sample are shown in Figure 1a. Vibrational modes consistent with oxygen-containing functionalities are apparent. At 300 K, vibrations due to carbonyl groups are detected at 1735 cm^{-1} and C–O type vibrations are seen at 1250 cm^{-1}. A very broad peak, which has previously been assigned to C=C vibration, is also seen at 1610 cm^{-1}.[17,18] These types of oxygen-derived functionalities have been seen in previous reports for carbon nanotube samples partially oxidized by a HNO_3/H_2SO_4 treatment.[17,19,42] Upon heating, a slight intensity decrease is seen in the 1735 cm^{-1} band accompanied by a frequency shifting toward 1690 cm^{-1}. Heating causes a slight intensity increase in the C–O band at 1250 cm^{-1} with shifting to 1220 cm^{-1} and the appearance of a new band occurs at 1080 cm^{-1}. The bands at 1220 and 1080 cm^{-1} are close in energy to bands previously assigned to asymmetric and symmetric modes, respectively, of esters on
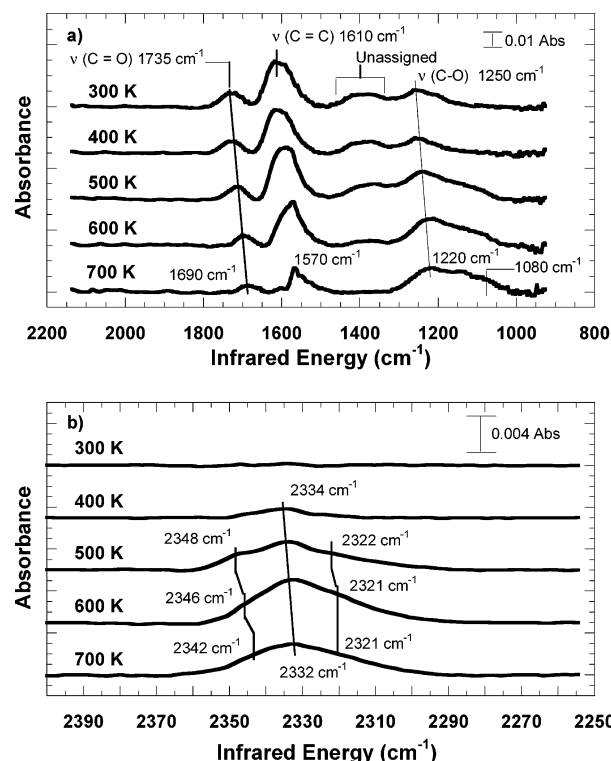

Figure 1. Infrared spectra of single-walled carbon nanotubes heated in a vacuum. (a) The partial decomposition of oxygen-related functionalities in the 800–2200 cm^{-1} region. (b) The appearance of a new vibration near the ν_3 mode of gaseous CO_2.

carbon nanotubes, while the band at 1690 cm^{-1} is close in energy to carbonyls associated with quinone functionalities.[18] Heating causes the C=C mode at 1610 cm^{-1} to lose intensity on its high energy side and to eventually become a very sharp feature at 1570 cm^{-1}. This sharp feature is evident in previous reports for carbon nanotubes heated to 723 K[17] and is likely related to the IR active nanotube phonon band at 1580 cm^{-1}. This phonon band becomes better defined after heating to ~1000 K.[17]

The IR changes seen in Figure 1a are consistent with a partial decomposition of oxygen-related functionalities on the nanotubes. After initial heating of the nanotube sample to 700 K, the changes shown in Figure 1a become permanent and persist without change over the temperature range of 5–700 K. The frequency shifts seen after heating for some of the vibrations suggest that in addition to partial decomposition there are structural changes occurring to the functionalities or to the defect sites with which they are associated.

Figure 1b shows IR spectra taken in the region near the ν_3 asymmetric stretching mode of CO_2 during heating. At 300 K, the IR spectra are featureless but at 400 K a vibrational mode becomes evident at 2334 cm^{-1} and at 500 K shoulders start to become apparent at 2348 and 2322 cm^{-1}. At higher temperatures, the peaks broaden and resolving each individual component becomes difficult. The decomposition of oxygen functionalities coupled with the appearance of a new IR band near the ν_3 frequency CO_2 in Figure 1b leads to the conclusion that the modes near 2330 cm^{-1} are due to CO_2 produced during the heating process. Previous studies have shown that CO_2 is generated during the heating of functionalized carbon nanotube samples.[17,30]

The frequency shift from the gas-phase seen for the ν_3 band in Figure 1b indicates a substantial interaction with the nanotube sample. By comparison, CO_2 adsorbed in powdered carbon has

Trapped CO$_2$ in Carbon Nanotube Bundles

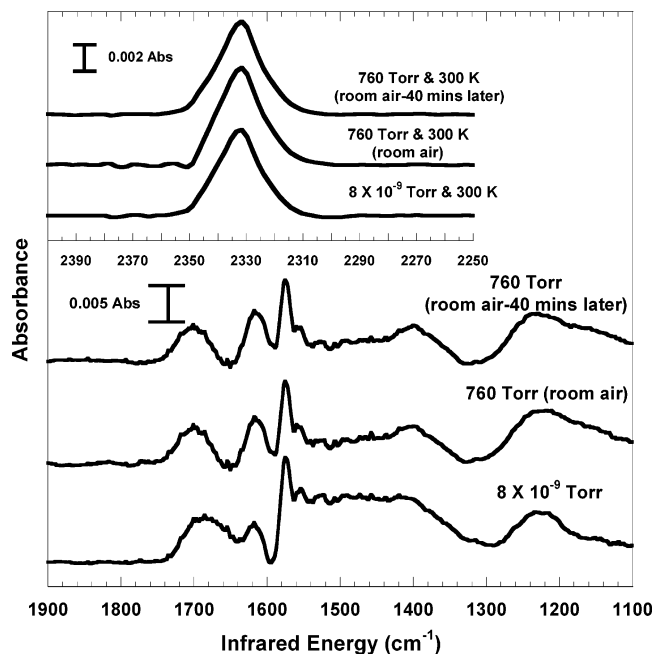*J. Phys. Chem. B, Vol. 107, No. 47, 2003* **12933**

Figure 2. Infrared spectra of single-walled carbon nanotubes heated in a vacuum and subsequently vented to room air. In the 1100−1900 cm^{-1} region, no significant changes are seen with oxygen-related functionalities except for a slight growth in the band at 1610 cm^{-1}. The inset shows the IR spectra in the 2250−2400 cm^{-1} region illustrating that the vibration at 2330 cm^{-1} persists even after exposure to room air.

a band near 2332 cm^{-1}.[29] In C$_{60}$ films there is a band reported at 2328 cm^{-1} [26,27] or 2331 cm^{-1} [26] depending on details of the film preparation.[26] CO$_2$ trapped in octahedral voids of a C$_{60}$ crystal has a vibration reported at 2332 cm^{-1} [23,28] and 2329 cm^{-1}.[28] CO$_2$ physisorbed on graphite displays a vibration at 2341 cm^{-1}.[27] The extremely wide range of carbons creating a ν_3 band near 2330 cm^{-1} is indeed surprising.

After the initial thermal heating, the features near 2330 cm^{-1} in Figure 1b become permanent bands in the IR spectra and do not disappear with time or upon temperature cycling from 5 to 700 K. These features do broaden and change in intensity in a reversible fashion during subsequent heating cycles (see below). These results show that the thermally induced functionality changes are stable and that some of the associated CO$_2$ generated during heating is trapped within the carbon nanotube bundle. The CO$_2$ trapped in our samples persists after multiple temperature cycles, and we have observed the ν_3 bands near 2330 cm^{-1} in samples for as long as 2 months in the vacuum chamber. Venting the vacuum chamber to room air and pressure (Figure 2) creates a slight intensity increase in the mode at 1610 cm^{-1} with the mode at 1690 cm^{-1} remaining unchanged in intensity and frequency. The bands near 2330 cm^{-1} also persist after venting of the chamber suggesting that CO$_2$ is indeed permanently trapped. Raman spectroscopy (Figure 3) of samples heated under vacuum and vented to room air display radial breathing modes characteristic of SWNTs. The Raman results prove that vacuum heating does not produce any drastic decomposition or rearrangement of the nanotube structure. The Raman spectra also show that the changes seen in the Fourier transform infrared spectra are confined to the functionalities decorating defects along the nanotube bundles and do not significantly alter the nanotube electronic structure.

To test whether the CO$_2$ trapped within these samples comes from the oxygen functionalities on the sample or trace amounts of CO$_2$ residing in the vacuum chamber, we have vacuum heated
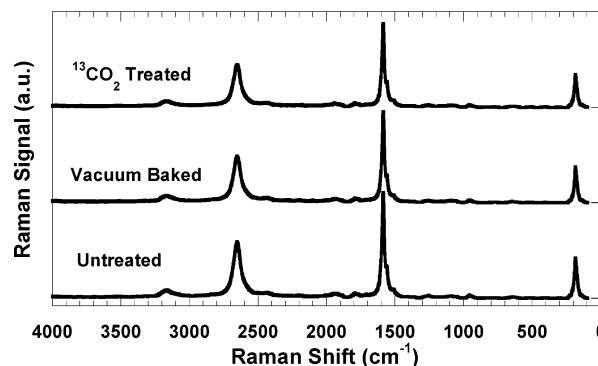

Figure 3. Raman spectra of untreated single-walled carbon nanotubes, vacuum heated nanotubes, and ^{13}CO$_2$ treated nanotubes. The characteristic radial breathing modes are apparent for all samples indicating that neither vacuum heating nor ^{13}CO$_2$ treatement results in any significant disruption of nanotube structure.
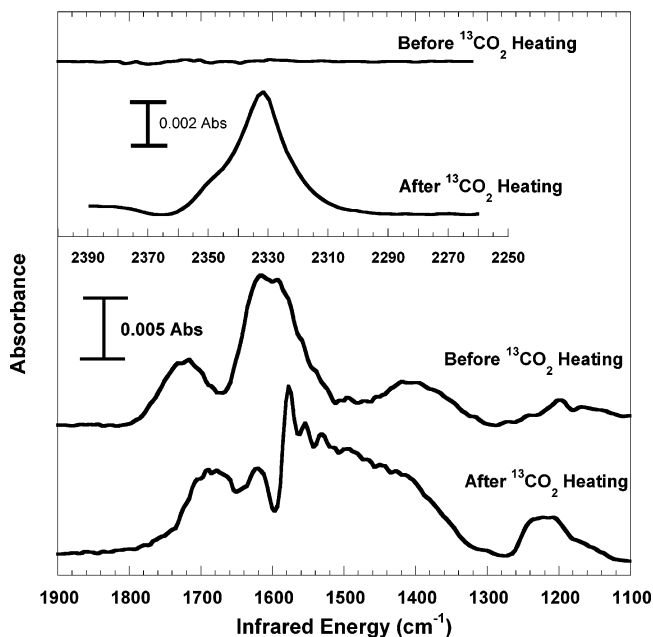

Figure 4. Infrared spectra of single-walled carbon nanotubes heated for 1 h in 8 × 10^{-4} Torr of ^{13}CO$_2$ at 700 K. Partial decomposition of oxygen-related functionalities is apparent in the IR of the 800−2200 cm^{-1} region. Few differences are apparent from the vacuum-heated sample shown in Figure 1. Inset shows the appearance of the ν_3 vibration near 2330 cm^{-1} after heating in ^{13}CO$_2$.

samples to 700 K in 8 × 10^{-4} Torr of ^{13}C enriched CO$_2$ for periods of about 1 h. The functionality changes for samples heated under ^{13}CO$_2$ are identical to those heated under a high vacuum (Figure 4). No evidence for trapped ^{13}CO$_2$ was found near the 2283 cm^{-1} ν_3 mode of the isotopically labeled gas. IR bands were observed for unlabeled CO$_2$ as seen in Figure 1b indicating that the trapped CO$_2$ does not come from adventitious CO$_2$ gas in the vacuum chamber.

IR spectra for the ^{13}CO$_2$ heated sample during venting are shown in Figure 5. Raman for this sample is displayed in Figure 3. The results are identical to those shown earlier for the vacuum-heated samples with the functionality changes and trapped CO$_2$ persisting even after exposure to atmosphere.

The changes in oxygen functionalities and generation of trapped CO$_2$ shown in these samples are not particular to the substrate or vacuum environment used in these experiments. Experiments run in the vacuum chamber using KBr windows as sample supports instead of CaF$_2$ also find trapped CO$_2$ in the nanotubes after heating to 700 K. Furthermore, samples
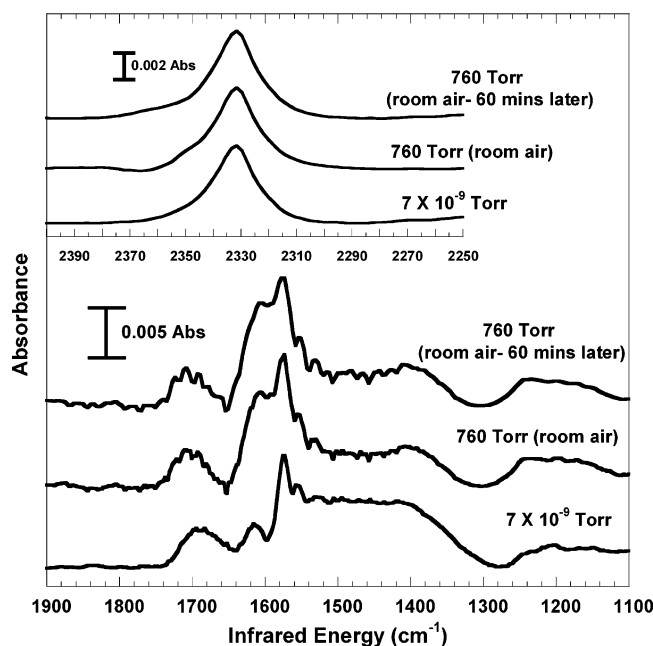
Figure 5. Infrared spectra of $^{13}CO_2$ treated single-walled carbon nanotubes during venting of the sample to room air. In the 1100–1900 cm^{-1} region, no significant changes are seen with oxygen-related functionalities except for a slight growth in the band at 1610 cm^{-1}. The noisy appearance of this spectrum is related to the incomplete background subtraction of atmospheric water vapor. Inset shows the 2250–2400 cm^{-1} region with the ν_3 vibration at 2330 cm^{-1} persisting even after exposure to room air.

heated to 673 K under ~250 atm of CH$_4$ in an autoclave cell also show the trapped CO$_2$ in their infrared spectra.

Temperature Dependence of the Trapped ν_3 Band. As mentioned above, the vibrational bands near 2330 cm^{-1} in thermalized samples persist at all temperatures and display reproducible intensity and line width variations as a function of temperature. The temperature dependence of the 2330 cm^{-1} mode is shown in Figure 6a for a vacuum-heated sample and in Figure 6b for a sample heated in 8×10^{-4} Torr of $^{13}CO_2$. At low temperatures, a prominent peak is seen near 2330 cm^{-1} with a high energy shoulder near 2340 cm^{-1}. Upon heating, these peaks broaden and a low energy shoulder starts to develop near 2320 cm^{-1}. At 550 K, the spectra evolve into what appears to be a single, broad, vibrational peak.

In an effort to understand the broadening and intensity changes seen in Figure 6, we have used 2D IR to analyze the data. The correlation spectra are given in Figure 7. The intensity of synchronous 2D spectra represents simultaneous changes of intensity, which occur at two independent spectral frequencies, ν_1 and ν_2, during heating. Simply put, if vibrational peaks in a set of spectra are coupled and experience simultaneous changes upon heating, then this should be reflected in the synchronous 2D spectra. Figure 7a shows a positive autopeak at ν_1/ν_2 of 2330/2330 cm^{-1} that corresponds to the loss of intensity seen at 2330 cm^{-1} upon heating. Also, a negative cross-peak is resolved at ν_1/ν_2 of 2318/2330 cm^{-1}. Negative cross-peaks indicate that the intensity at one spectral variable is increasing while the intensity at the other variable is decreasing. In this particular case, the autopeak represents the decreasing intensity of the central 2330 cm^{-1} peak coupled with the increasing intensity of the low energy shoulder at 2320 cm^{-1}.

Asynchronous correlation spectra are also shown in Figure 7b. Peaks in the asynchronous spectra represent sequential changes that occur between bands in spectra. Asynchronous spectra are particularly useful in resolving overlapping bands
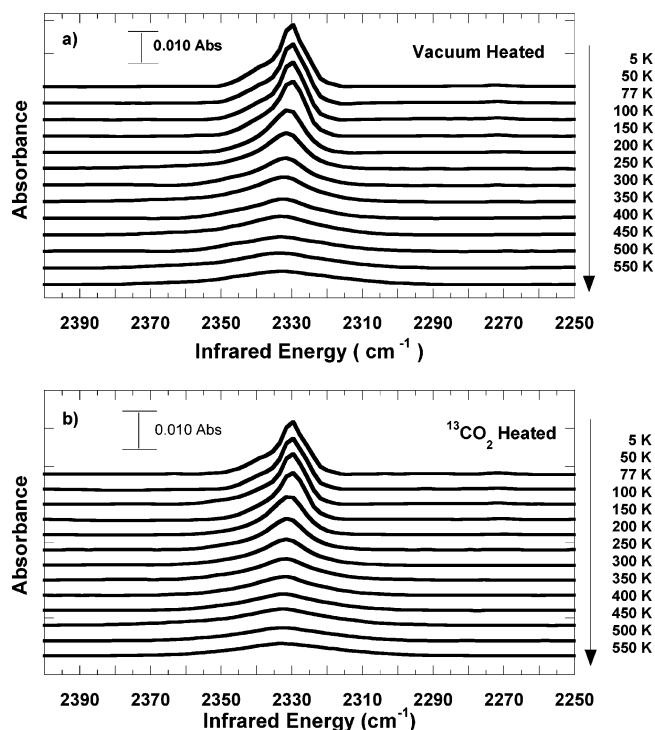

Figure 6. Temperature dependence of the ν_3 mode of CO$_2$ trapped within single-walled carbon nanotube bundles. (a) Infrared spectra in the region of 2250–2400 cm^{-1} for a vacuum-heated sample. Spectra are intentionally offset on the y-axis for clarity. (b) Infrared in the same region as (a) but for a sample heated in $^{13}CO_2$. Again, y-axis offset is introduced for clarity.

of different origin in spectra. The asynchronous spectra show cross-peaks at 2330/2340 cm^{-1} and at 2320/2330 cm^{-1}. This suggests that in addition to the clearly resolved feature at 2330 cm^{-1} in Figure 7, the shoulders at 2340 and 2320 cm^{-1} arise from distinct vibrational bands. This is also convincingly demonstrated by noting that the bands at 2320, 2330, and 2340 cm^{-1} are fairly well resolved in the spectra of Figure 1b.

The bands observed at 2340, 2330, and 2320 cm^{-1} suggest that there are three distinct environments accessible to CO$_2$ within the nanotube bundles. Using these three distinct vibrational features, we fitted the IR spectra with three Lorenztians and extracted the integrated area, the resonance frequency, and line width of each peak as a function of temperature.

The resonance frequency of each mode is shown in Figure 8a as a function of temperature. The vibrational frequencies of the bands near 2340 and 2330 cm^{-1} increase with temperature from 2336 to 2342 cm^{-1} and from 2329 to 2333 cm^{-1}, respectively. The frequency variation with temperature for both these modes is approximately linear. The mode near 2320 cm^{-1} shows no real frequency shifting upon heating.

Figure 8b shows that each mode broadens in an approximately linear fashion as a function of temperature. This broadening is, in part, what makes the IR spectra at higher temperatures look more like a single broadened vibrational feature rather than three distinct, resolved features.

The integrated areas for each deconvoluted vibration are shown in Figure 9a and 9b. The feature at 2330 cm^{-1} displays a strong decrease in its integrated area while the feature at 2320 cm^{-1} displays an increase. Below ~300 K, the integrated area of the 2320 cm^{-1} mode becomes negligible. The band at 2340 cm^{-1} shows a decrease in integrated area upon heating. One striking feature of Figure 9 is the decrease of total integrated intensity from 2250 to 2390 cm^{-1} upon heating. This intensity
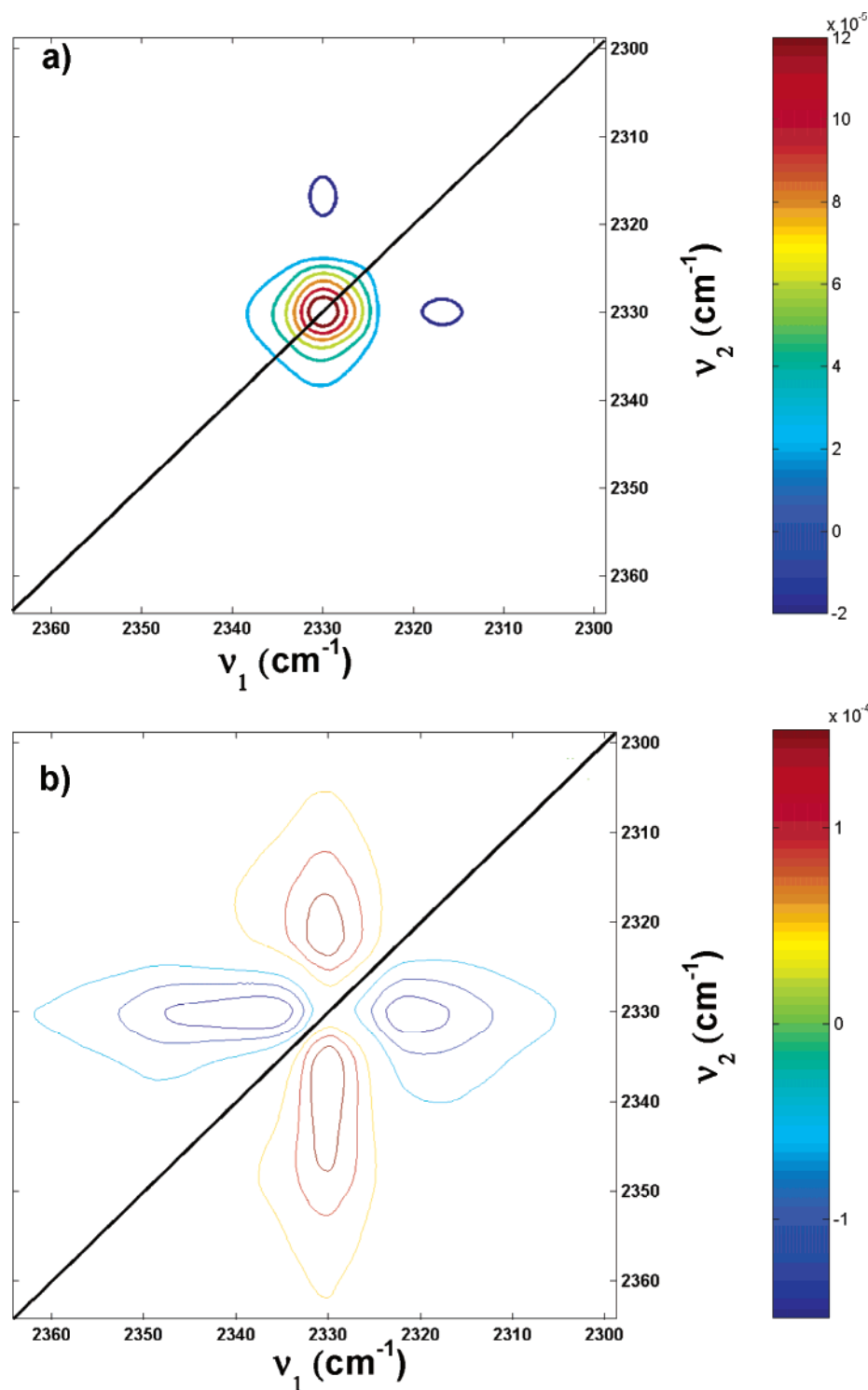
Trapped CO$_2$ in Carbon Nanotube Bundles

J. Phys. Chem. B, Vol. 107, No. 47, 2003 **12935**

Figure 7. Two-dimensional correlation spectra displaying the temperature-induced changes in the ν_3 mode of CO$_2$ trapped within the nanotube bundles. (a) Synchronous spectra for sample where trapped CO$_2$ is produced by vacuum heating to 700 K. (b) Asynchronous spectra for sample from (a). Two-dimensional correlation spectra for ^{13}CO$_2$ heated samples show similar results.

loss is reversible and reproducible over successive temperature cycles (Figure 9b). No new CO$_2$ is introduced between temperature cycles so the intensity variations occur from a physical process, not from the loss of trapped CO$_2$ during heating. The factor of ~2 change seen in the integrated intensity for each of the vibrations during heating indicates an ~$\sqrt{2}$ change in the dynamic dipole moment, $(\partial\mu/\partial Q_i)$,[43,44] of trapped CO$_2$. This change is likely related to the temperature-dependent interactions of the trapped CO$_2$ molecule with the nanotube bundle, which we examine through computer simulations below.

We use canonical simulations (*NVT* ensemble) of CO$_2$ trapped in the interior of single-walled nanotubes and in the interstitial channels of nanotube bundles to investigate possible causes for the temperature dependence of the IR peaks and to extract the basic physics of the trapped CO$_2$ species. For the vacuum-heated samples, the CO$_2$ molecules are trapped in the interior and interstitial sites (see discussion below); thus, we use a heterogeneous bundle in the calculations since GCMC simulations indicate that CO$_2$ does not adsorb in the interstitial channels of close-packed homogeneous nanotubes. We have computed the
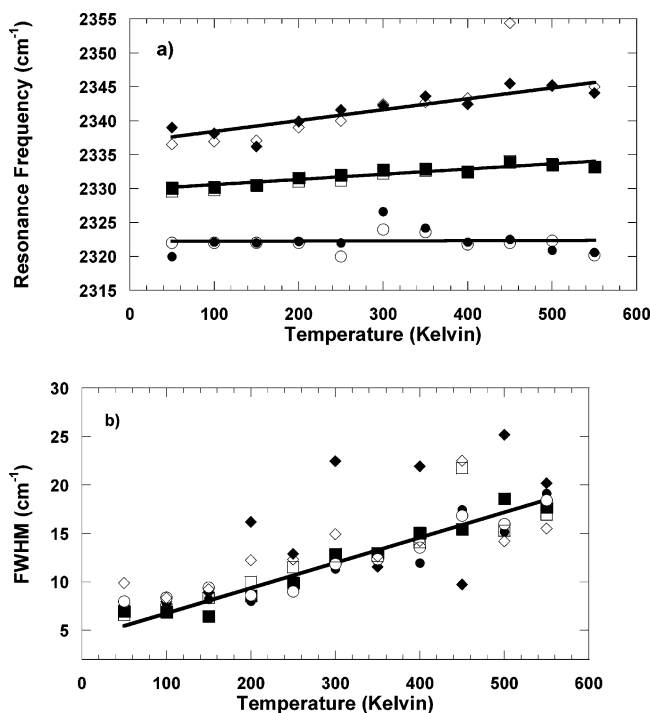
Figure 8. Temperature dependence of spectral parameters from the 3 Lorenztian line shape fit. (a) Temperature dependence of the resonance frequency for the mode near 2320 cm^{-1} (solid and open circles), 2330 cm^{-1} (solid and open squares), and 2340 cm^{-1} (solid and open diamonds). Solid symbols correspond to the vacuum-heated sample and open symbols to the $^{13}CO_2$ treated sample. (b) Effect of temperature on the line width of the 3 Lorenztian features [same key as (a)].

potential energy distribution for CO_2 trapped inside heterogeneous nanotube bundles (bundles 1 and 2 from Table 2) at endohedral and interstitial sites at a constant coverage as a function of temperature. Figure 10a and 10b present the results for endohedral and interstitial sites, respectively. At low temperatures, CO_2 molecules are essentially trapped in the sites with the highest binding energies, as seen by the sharply peaked potential energy distribution. As the temperature increases, the CO_2 molecules move more freely in phase space and have a much larger probability of occupying sites with lower binding energy, which results in broader energy distributions with increasing temperature, as shown in Figure 10. If we assume that the IR shift is roughly proportional to the binding energy, then the broadening and intensity decrease of the 2330 and 2340 cm^{-1} peaks can be understood as the result of CO_2 molecules escaping from a tightly bound solidlike adsorbed phase to a freer, gaslike phase that is much less strongly bound to the surface. This change of state can be seen more clearly in Figure 11, which shows the density profiles inside a (10,10) nanotube at the same coverage as in Figure 10a. At the lowest temperature, the CO_2 molecules are mostly packed against the walls of the nanotube, shown as the first peak on the right in Figure 11. The smaller second peak on the right arises from configurations where the CO_2 molecules are closely packed together in such a way that some molecules are not parallel with the nanotubes axis, thus shifting their center of mass out slightly from the tube wall. This orientational ordering is due to quadrupole–quadrupole interactions and will be discussed in terms of groove site adsorption in more detail later. There is also a small peak for CO_2 molecules in the center of the tube shown by the peak at $r = 0$ for 100 K. This annular CO_2 occurs because the molecules form solidlike clusters rather than having uniform density down the length of the tube. As the temperature increases
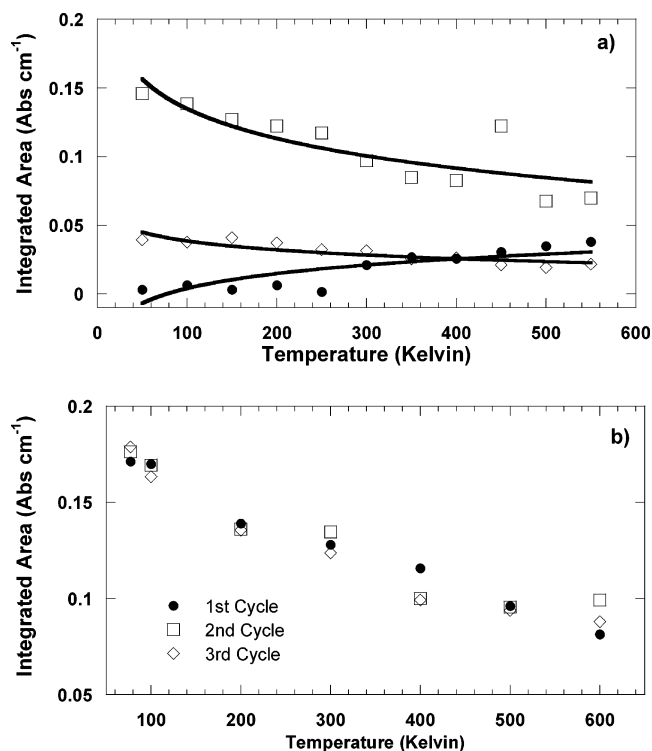

Figure 9. Temperature dependence of integrated intensity of the trapped ν_3 mode. (a) integrated area of the Lorenztian near 2320 cm^{-1} (solid circles), 2330 cm^{-1}(open squares), and 2340 cm^{-1} (open diamonds). For clarity only, results from the $^{13}CO_2$ heated sample are shown, but vacuum-heated samples show the same trends. Solid lines are only meant as a guide to the eye. (b) Total integrated intensity change for the region 2250−2390 cm^{-1} during multiple temperature cycles.
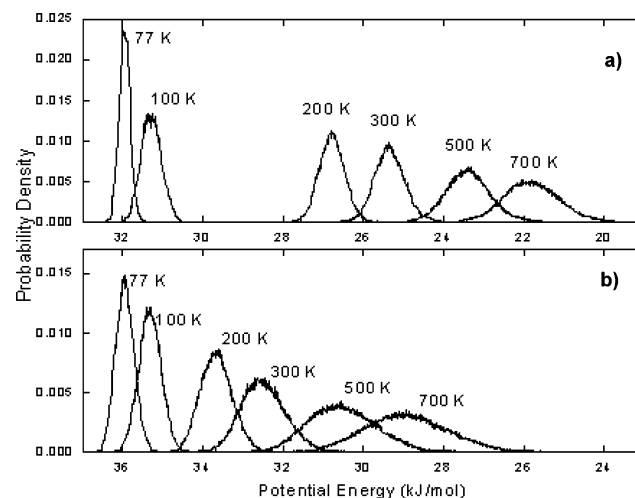

Figure 10. Potential energy distributions as a function of temperature. (a) For CO_2 trapped in the interior of a (10,10) nanotube. (b) For CO_2 trapped in the interstitial regions of a heterogeneous nanotube bundle.

the structure disappears; the density next to the wall decreases and the second and third peaks disappear. At very high temperatures, the fluid is almost uniformly distributed across the radius of the nanotube, indicating a gaslike phase confined within the tube that is still perturbed by interactions with the nanotube adsorption potential.

　Note the presence of a large gap in energy distributions between 100 and 200 K in Figure 10a. This feature is indicative of a phase transition from a condensed phase of CO_2 to a gaslike phase inside the nanotube. For comparison, the triple point of bulk CO_2 is 216.58 K, with a pressure of 5.2 bar. There is no
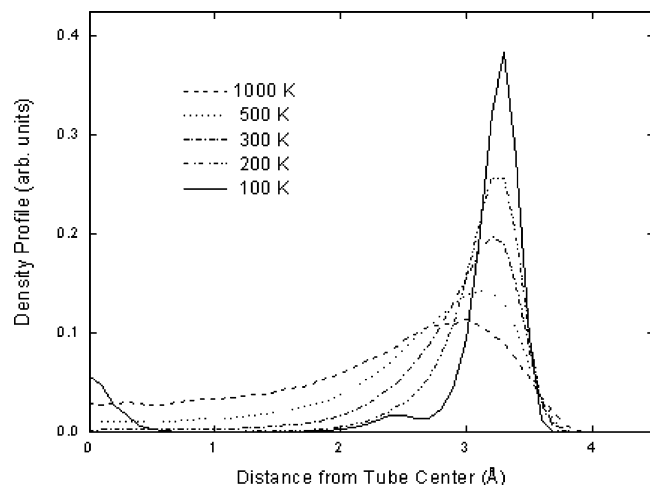
Trapped CO₂ in Carbon Nanotube Bundles

J. Phys. Chem. B, Vol. 107, No. 47, 2003 **12937**

Figure 11. Density profiles for CO_2 trapped inside a (10,10) nanotube at constant coverage of 0.16 molecules per Angstrom as a function of temperature.
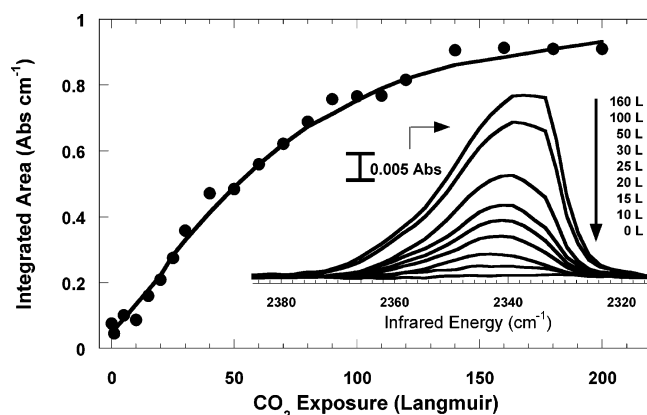

Figure 12. CO_2 dosing experiments for an untreated nanotube sample. The infrared spectra as a function of CO_2 exposure are shown as an inset. The integrated area of the infrared band is determined numerically from the data represented in the inset. For clarity, not all of the infrared spectra are shown in the inset, but all CO_2 exposures are used in the main figure. Solid line in the main figure is a guide to the eye.

such energy gap for CO_2 in the small interstitial sites because the interstitial channels are more strongly confined and more closely correspond to a true one-dimensional system (i.e., no first-order phase transitions). The interior of a (10,10) nanotube is large enough to exhibit quasi-two-dimensional behavior.

Gas-Phase CO_2 Adsorption in Untreated and Vacuum-Heated Samples. In addition to generating trapped CO_2, it is reasonable to expect that thermolysis should result in some CO_2 that escapes. In this scenario, vacuum heating of samples should partially open the nanotube bundles to adsorption of external gas in addition to the CO_2 species that become trapped within the bundle. The new sites generated for external gas adsorption would likely be similar to those accessed by the trapped CO_2.

To test this hypothesis, adsorption studies were done by exposing untreated and vacuum-heated samples at 77 K to CO_2 gas in units of langmuir (L; 1 L = 1 × 10^{-6} Torr-sec). The results for a nanotube sample before thermolysis are shown in Figure 12. The untreated sample shows a single vibration which gains intensity as the sample is dosed. This band is broad and has a peak frequency of $\sim$2342 cm^{-1} at low coverage and shifts to $\sim$2336 cm^{-1} at higher coverage. The integrated intensities for these spectral data are also shown in Figure 12. The intensity of this vibration starts to grow almost immediately and continues until reaching a plateau at $\sim$140 L of CO_2 exposure. This plateau
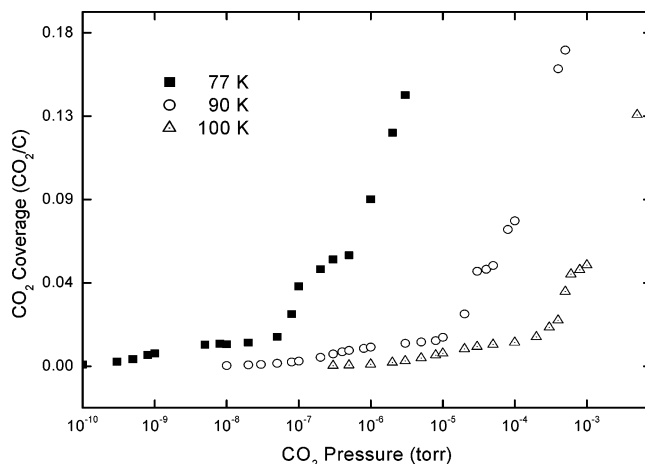

Figure 13. Adsorption isotherms at 77, 90, and 100 K for CO_2 on a closed perfect bundle of 9 (10,10) nanotubes.

is consistent with the filling of all available sites for CO_2 adsorption. Since only one infrared vibration is detected at $\sim$2340 cm^{-1}, CO_2 is presumably adsorbed in one single type of site.

Figure 13 presents the simulation results for CO_2 adsorption isotherms on the closed perfect bundle (bundle 3 in Table 2) at temperatures ranging from 77 to 100 K. These results are directly comparable to the experimental data for CO_2 adsorption on untreated SWNT bundles (see Figure 12). The closed perfect bundle is used to approximate groove site and external surface adsorption on the untreated tubes since the functionalities on these tubes will effectively block access to interior sites of the bundle.

The isotherms in Figure 13 each contain two plateaus. Each plateau corresponds to the filling of a certain type of site on the exterior of the nanotube bundle. Groove site filling corresponds to the first plateau in the isotherms shown in Figure 13. Analysis of simulation snapshots shows that quadrupole−quadrupole interactions force CO_2 molecules to form a T-shaped one-dimensional chain in the groove, as shown in Figure 14, top panel. Analysis of simulation snapshots at lower pressures show that a low-density adsorbed phase forms first, where the CO_2 molecules are well separated and have their axes aligned with the groove axis to maximize their van der Waals interactions with the tubes making up the groove. As the pressure increases, the distance between the CO_2 molecules in a single groove gets smaller and the molecules experience competing effects of repulsive quadrupole−quadrupole interactions and attractive dispersion interactions between a pair of CO_2 molecules. Roughly speaking, at close packing every other CO_2 molecule rotates up, with its molecular axis perpendicular to the direction of the groove to make the quadrupole−quadrupole interactions attractive. This behavior is shown for a snapshot from a simulation at 90 K in Figure 14. Snapshots from isotherms at 77 and 100 K also show this behavior for loadings corresponding to groove site filling. The lower panel in Figure 14 is a snapshot of CO_2 adsorbed in an interstitial site from bundle 1 (see Table 2). Only three of the five tubes making up the interstitial site are shown to facilitate viewing of the CO_2 molecules. The configurations adopted by CO_2 in this interstitial site are clearly very similar to those in the groove site in the top panel.

The second plateau appearing on each of the isotherms in Figure 13 corresponds to the formation of a monolayer film. These films begin to form at about 10^{-7}, 3 × 10^{-5}, and 6 × 10^{-4} Torr at 77, 90, and 100 K, respectively. A contour density
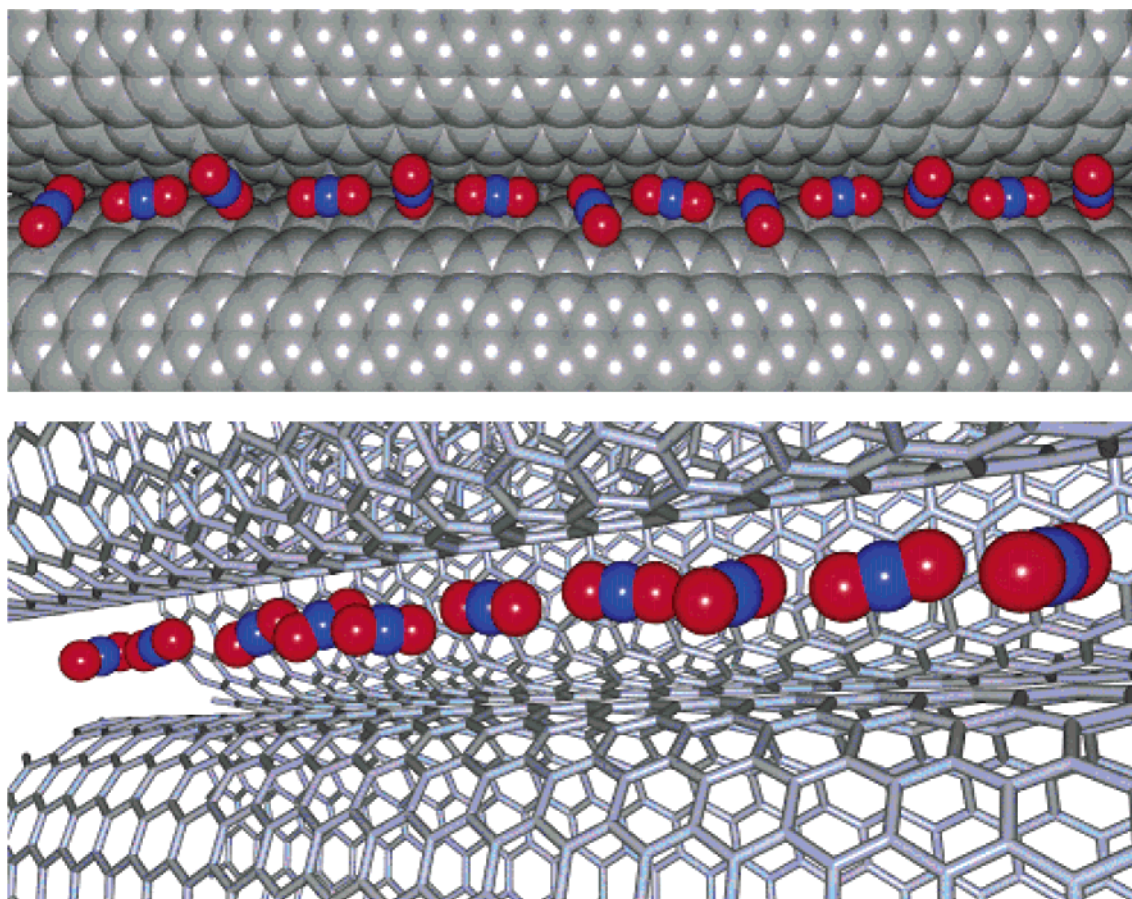
Figure 14. (top) Snapshot of CO_2 adsorption in a single groove site on a closed perfect bundle of 9 (10,10) nanotubes at 90 K and 3×10^{-6} Torr. Snapshots at other temperatures display similar structures at groove filling. Red spheres are oxygen atoms, blue spheres represent carbon in CO_2, and gray spheres represent carbon in the nanotubes. (bottom) Snapshot of CO_2 adsorption in an interstitial site of bundle 1 from Table 2. The carbons in the nanotubes are shown in wire frame to make the adsorbed CO_2 molecules visible. Most of the tubes in the bundle have been excluded from the figure for clarity.
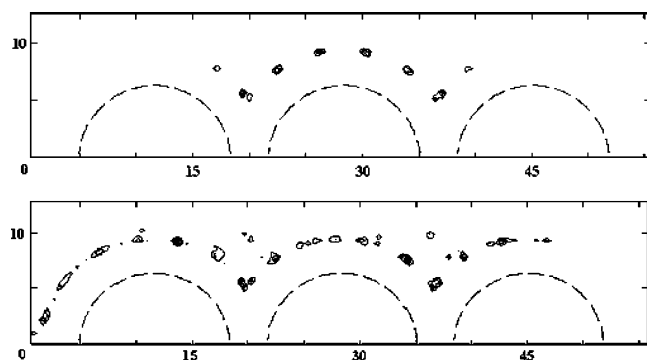

Figure 15. Density contours for CO_2 adsorbed on the external surface of a perfect bundle consisting of 9 (10, 10) nanotubes. Two groove sites are shown, along with the surface of the three tubes making up one side of the bundle. The central tube is located in the center of one edge of the nanotubes bundle. The upper panel corresponds to a coverage of 0.055 molecule/carbon atom and the lower panel to a coverage of 0.1 molecule/carbon atom. Individual nanotubes are represented as dashed lines.

plot showing a close up of the bundle surface is plotted in Figure 15. The top panel corresponds to the monolayer plateau region. However, the entire surface of the bundle is not actually covered. Heterogeneity in the coverage is due to nanotubes at the corners of the bundle having a slightly different potential energy surface than nanotubes midway along the edge. This heterogeneity is in contrast with the work of Cole et al.[7,45,46] who used a model of a periodic slab of nanotubes, so that each nanotube was

exactly equivalent to any other one on the surface. The type of model used by Cole and co-workers gives sharp transitions similar to layering transitions on graphite. Our results show that even a perfect homogeneous bundle introduces enough heterogeneity into the problem to make the transitions appear continuous rather than first order. A bilayer film begins to form past the second plateau regions on each of the isotherms shown in Figure 13. The density contours are shown in Figure 15 in the lower panel. Note that the bilayer begins to form over the groove site first and that the outside corner of the bundle (right side) is still not completely covered with a monolayer film. Thus, the bilayer begins to form before the monolayer is complete on the nanotubes at the corners of the bundle. This means that the experimental vibrational spectra are not expected to show distinct changes with increased exposure. The spectra should gradually broaden and shift as the coverage increases. This is precisely what is observed in the experiments (see Figure 12). We do not observe a clear second-layer groove phase or three-stripe phase as observed by Cole et al.[7,45,46] We believe that this is due to our using a small finite bundle rather than an infinite row of nanotubes.

Experimentally, CO_2 adsorption in the vacuum-heated sample (Figure 16a) is somewhat different from the untreated tubes described above. Since this sample has been heated to 700 K, it contains trapped CO_2 and its spectra display a ν_3 band even before CO_2 exposure. Upon CO_2 dosing, the shoulder at $\sim$2340 cm^{-1} starts to gain intensity and grows with continued dosing. Associated with this is the apparent growth of the peak at 2330

Trapped CO$_2$ in Carbon Nanotube Bundles

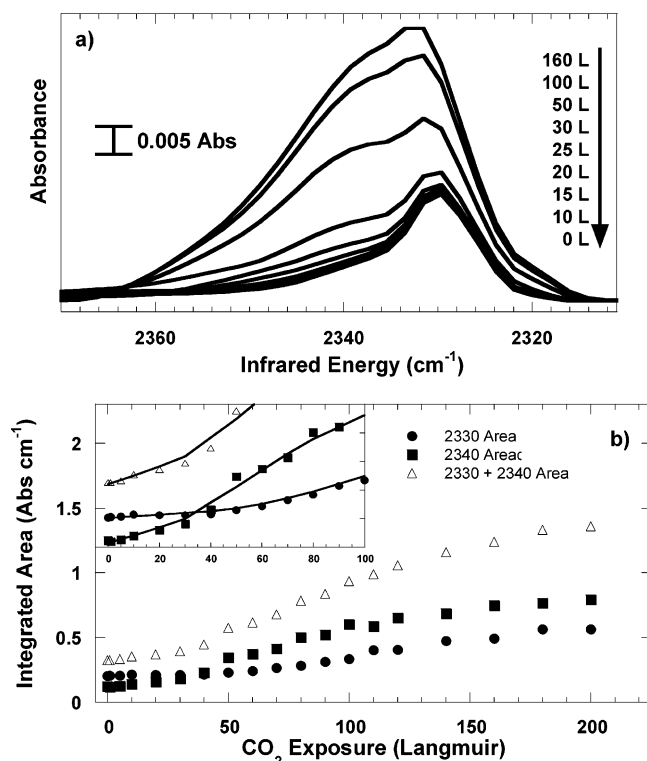*J. Phys. Chem. B, Vol. 107, No. 47, 2003* **12939**

Figure 16. CO$_2$ dosing experiments for a nanotube sample subjected to heating at 700 K. (a) Infrared spectra as a function of CO$_2$ exposure. (b) Integrated area of the infrared band determined from deconvoluting the band in (a) as 2 Lorenztians. Inset of (b) is an enlargement of the region below 100 L showing the sequential filling of adsorption sites mentioned in the text.

cm^{-1}. To separate the different contributions to these intensity changes, the spectra in Figure 16a are deconvoluted with a 2 Lorenztian fit and the integrated intensities are plotted in Figure 16b. Attempts to include a third Lorentzian near 2320 cm^{-1} were unsuccessful and from Figure 9a the intensity contribution from this mode is negligible at the temperature used for CO$_2$ dosing.

In Figure 14b (inset), the intensity of the 2340 cm^{-1} mode increases immediately at low doses while the 2330 cm^{-1} vibration does not gain appreciable intensity growth until ~40 L of CO$_2$ exposure suggesting a sequential filling of adsorption sites. The integrated intensity of the 2340 cm^{-1} mode starts to plateau at ~120 L indicating a filling of these adsorption sites and the mode at 2330 cm^{-1} just begins to plateau at ~170 L.

The filling of the sites at 2330 cm^{-1} in the vacuum-heated sample indicates that heating creates adsorption sites for gas-phase CO$_2$ not accessible in the untreated nanotube sample. The IR frequency of this adsorbed species is similar to the 2330 cm^{-1} frequency seen for trapped CO$_2$ suggesting that CO$_2$ adsorbed from the gas phase is accessing a similar local environment as trapped CO$_2$. Likewise, the vibration at 2340 cm^{-1} for trapped CO$_2$ is similar in frequency to the bands seen after exposing CO$_2$ to both vacuum-heated and untreated nanotube samples suggesting that trapped and adsorbed CO$_2$ are accessing similar local environments.

To understand the results of Figure 16, we consider adsorption simulations of CO$_2$ on interstitial and internal sites of a heterogeneous nanotube bundle. Results of GCMC simulations on bundle 1 (see Table 2) are plotted in Figure 17. At low pressures (see the inset to Figure 17), the smallest interstitial sites fill first, followed by adsorption inside the nanotubes and the larger interstitial sites. The interstitial sites fill continuously
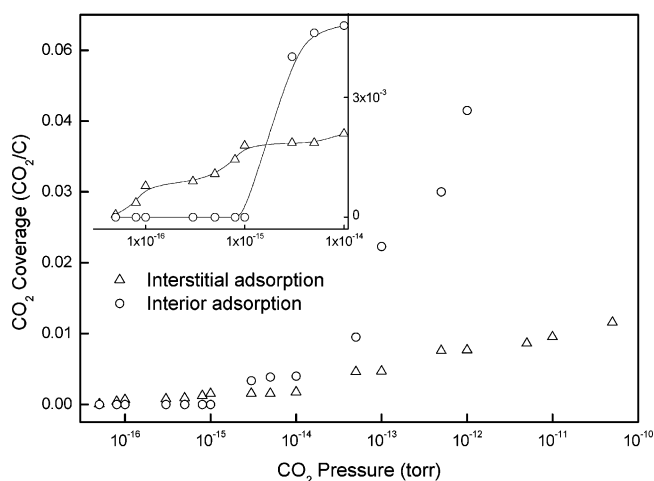

Figure 17. Adsorption isotherm at 77 K on a heterogeneous bundle. The inset shows the low pressure region. Gas initially adsorbs in the interstitial channels formed by nanotube packing defects, then into the open nanotubes.

over a very wide pressure range because there are several different interstitial sites, each having different binding energies and capacities. This qualitatively matches the experimental observations from dosing CO$_2$ on the heated nanotubes (see Figure 16), which also shows sequential filling of sites. This result suggests that the 2340 cm^{-1} mode, which fills first experimentally, is attributable to interstitial adsorption and the 2330 cm^{-1} mode, which fills next, is due to internal adsorption. Further arguments for these band assignments are made below using other experimental evidence. The quantitative differences between experiments and simulations may stem from the fact that in the experimental situation only a small fraction of the interstitial sites and nanotubes are opened enough to allow gas adsorption.

Assigning Adsorption Sites for the ν_3 Bands. Assigning vibrational bands to particular adsorption sites can be a tricky task in heterogeneous samples such as carbon nanotubes. Arguments for certain sites can be made on the basis of all of the experimental and computational information available from this study. These assignments are tentative and are based on currently available data. Further experimentation and computational studies will be needed to make these assignments definitive.

In a nanotube bundle, adsorption can occur in groove sites, interstitial sites, inside the tube, and on the curved outer surface of the nanotube. The only logical adsorption sites that can occur for the trapped CO$_2$ species are interstitial sites and sites inside the nanotube. On the basis of this, the bands seen at ~2340 cm^{-1} and ~2330 cm^{-1} for trapped CO$_2$ (Figure 6) must arise from either of these two sites. It is later argued that the mode at 2340 cm^{-1} comes from CO$_2$ in interstitial sites and the 2330 cm^{-1} vibration from CO$_2$ inside the nanotubes.

Adsorption on unheated nanotubes creates a single band at ~2340 cm^{-1} (Figure 12) which is similar to the one seen for trapped CO$_2$ (Figure 6). This band must arise from a site with a similar enough local environment to produce the ν_3 frequency of ~2340 cm^{-1} for both cases. The only site of similar nature on both the exterior and the interior of a bundle are the groove and larger interstitial sites, respectively. In both cases, a V-shaped channel is created between adjacent nanotubes. Intuitively, a CO$_2$ molecule will lie lengthwise in the V-shaped channel to maximize its van der Waals interactions with the nanotube. Our simulations show that at high coverage the CO$_2$ molecules rotate with respect to one another to facilitate an

attractive quadrupole−quadrupole interaction (see Figure 14). We therefore expect the local environment, particularly at low temperatures, to be nearly identical for both cases. The simulation snapshots of Figure 14 support this argument by showing that the adsorption geometry for both the groove and interstitial sites are similar. On the basis of this argument, we assign the 2340 cm^{-1} band for the trapped CO_2 of Figure 6 to CO_2 in interstitial channels. The 2340 cm^{-1} band of physisorbed CO_2 in unheated tubes (Figure 12) is assigned to groove sites on the exterior of the bundle. Assigning the 2340 cm^{-1} mode to interstitial adsorption for trapped CO_2 forces the assignment of the 2330 cm^{-1} mode for trapped CO_2 (Figure 6) to sites within the interior of the nanotube itself (endohedral).

Heating of the nanotube bundle creates a partial decomposition of chemical functionalities (Figure 1), which block access to interior sites of the bundle. This is seen in adsorption experiments on unheated (Figure 12) and heated (Figure 16) samples, which display different adsorption sites. Adsorption of gas-phase CO_2 on the heated nanotubes increases the intensity of the ν_3 bands of the trapped CO_2 species suggesting that the gas-phase molecules are accessing identical sites as the trapped species. This suggests that in addition to trapping CO_2 in interstitial and endohedral sites, thermolysis also partially opens the nanotubes for CO_2 adsorption. The adsorption data of Figure 16 show that the 2340 cm^{-1} band, which was assigned above to interstitial sites for trapped CO_2, grows before the 2330 cm^{-1} band assigned to endohedral adsorption. In addition to the earlier arguments for assignment of these bands, this sequential filling is also seen in the adsorption simulations displayed in Figure 17. This serves as another piece of evidence for these particular band assignments.

The similarity in frequency between the 2340 cm^{-1} modes from the current study and the 2340 cm^{-1} seen for CO_2 adsorption on graphite[27] tempts one to assign this peak to CO_2 physisorbed on graphitic-like carbon in the nanotube samples. We rule out CO_2 on graphitic carbon as a source for this peak in the nanotube samples since we observe contributions from the 2340 cm^{-1} band for trapped CO_2 over the entire temperature range (5−700 K) of this study. If graphitic carbon were the adsorbent for the trapped CO_2 species at 2340 cm^{-1}, heating in this manner would result in desorption from the graphite surface and a complete loss of intensity from the 2340 cm^{-1} mode.

The mode seen at 2320 cm^{-1} is difficult to assign. Since this mode is only seen during heating, it is possibly related to CO_2 diffusing into higher energy sites inside the tubes and interstitial pores. The simulation results of Figure 10 show this scenario by demonstrating how heating increases the ability of trapped CO_2 to sample phase space and access higher energy binding sites within both the nanotube and interstitial pores. Another possible cause for the 2320 cm^{-1} peak is that it is an artifact due to broadening of the central 2330 cm^{-1}. Currently, we are unable to make a strong argument for the origin of the 2320 cm^{-1} mode.

As mentioned earlier, many different types of carbon produce adsorbed[26,27,29] and trapped CO_2 species[23,28] with vibrational frequencies similar to those observed in this study. This suggests that the frequency shifting from the gas phase seen for these species has a complicated dependence on the details of the CO_2 interaction with its adsorbent. The nanotube samples used in this study are of high quality and most of the unwanted carbons are removed by the acid purification procedure.[32] It seems highly unlikely that the effects we see in the current study can be solely due to any carbon impurities in our sample.

The idea of using trapped gases to help assign peaks for IR studies of gas adsorption in carbon nanotubes is interesting. The current study is restricted to CO_2 generated by the sample itself, but there is no fundamental reason other gases cannot be adsorbed in opened nanotube bundles and then sealed by some chemical or physical procedure. If this procedure were successful, then studies similar to what has been reported here could be carried out and the similarities/differences between trapped and adsorbed species could be used to help facilitate band assignments. It may also be possible to re-functionalize the defect sites so that other types of gases besides CO_2 are produced and trapped during thermolysis. This approach offers another means to trap gas in nanotube bundles without the extremes of pressure and heat.[47]

Summary

Thermolysis of oxygen-containing functionalities on carbon nanotubes can create CO_2 that becomes permanently trapped in the nanotube bundles. The decomposition of these functionalities and subsequent trapping of CO_2 was studied with infrared spectroscopy. The ν_3 band of trapped CO_2 is red shifted from the gas phase to ∼2330 cm^{-1} with a high energy shoulder at 2340 cm^{-1}. At high temperatures, there is evidence for another shoulder at 2220 cm^{-1}. Computer simulations of the trapped CO_2 species show drastic changes in the binding energy distributions and density profiles, which qualitatively explain the frequency shifting, broadening, and integrated intensity changes observed in the infrared spectra. Computer simulations and experiments point to sequential filling of sites for gas-phase CO_2 adsorption on heated tubes with small defect interstitial sites filling before endohedral sites. The limited number of sites available for trapped CO_2 in nanotube bundles is used to facilitate tentative assignments for each of the infrared bands.

References and Notes

(1) Stan, G.; Cole, M. W. *Surf. Sci.* **1998**, *395*, 280.
(2) Stan, G.; Bojan, M. J.; Curtarolo, S.; Gatica, S. M.; Cole, M. W. *Phys. Rev. B* **2000**, *62*, 2173.
(3) Wang, Q.; Challa, S. R.; Sholl, D. S.; Johnson, J. K. *Phys. Rev. Lett.* **1999**, *82*, 956.
(4) Simonyan, V. V.; Johnson, J. K.; Kuznetsova, A.; Yates, J. T. *J. Chem. Phys.* **2001**, *114*, 4180.
(5) Ayappa, K. *Langmuir* **1998**, *14*, 880.
(6) Mao, Z.; Sinnott, S. B. *J. Phys. Chem. B* **2000**, *104*, 4618.
(7) Gatica, S. M.; Bojan, M. J.; Stan, G.; Cole, M. W. *J. Chem. Phys.* **2001**, *114*, 3765.
(8) Bhide, S. Y.; Yashonath, S. *J. Chem. Phys.* **2002**, *116*, 2175.
(9) Bienfait, M.; Asmussen, B.; Johnson, M.; Zeppenfeld, P. *Surf. Sci.* **2000**, *460*, 243.
(10) Muris, M.; Dufau, N.; Bienfait, M.; Dupont-Pavlovsky, N.; Grillet, Y.; Palmari, J. P. *Langmuir* **2000**, *16*, 7019.
(11) Muris, M.; Dupont-Pavlovsky, N.; Bienfait, M.; Zeppenfeld, P. *Surf. Sci.* **2001**, *492*, 67.
(12) Talapatra, S.; Krungleviciute, V.; Migone, A. D. *Phys. Rev. Lett.* **2002**, *89*, 246106.

Trapped CO$_2$ in Carbon Nanotube Bundles

J. Phys. Chem. B, Vol. 107, No. 47, 2003 **12941**

(13) Talapatra, S.; Migone, A. D. *Phys. Rev. B* **2002**, *65*, 045416.

(14) Talapatra, S.; Zambano, A. Z.; Weber, S. E.; Migone, A. D. *Phys. Rev. Lett*. **2000**, *85*, 138.

(15) Weber, S. E.; Talapatra, S.; Journet, C.; Zambano, A. Z.; Migone, A. D. *Phys. Rev. B* **2000**, *61*, 13150.

(16) Mawhinney, D. B.; Yates, J. T. *Carbon* **2001**, *39*, 1167.

(17) Kuznetsova, A.; Mawhinney, D. B.; Naumenko, V.; Yates, J. T.; Liu, J.; Smalley, R. E. *Chem. Phys. Lett*. **2000**, *321*, 292.

(18) Mawhinney, D. B.; Naumenko, V.; Kuznetsova, A.; Yates, J. T. *J. Am. Chem. Soc*. **2000**, *122*, 2383.

(19) Mawhinney, D. B.; Naumenko, V.; Kuznetsova, A.; Yates, J. T.; Liu, J.; Smalley, R. E. *Chem. Phys. Lett*. **2000**, *324*, 213.

(20) Byl, O.; Kondratyuk, P.; Forth, S.; Fitzgerald, S.; Yates, J. T. *J. Am. Chem. Soc*. **2003**, *125*, 5889.

(21) Byl, O.; Kondratyuk, P.; Yates, J. T. *J. Phys. Chem. B* **2003**, *107*, 4277.

(22) Williams, K. A.; Bhabendra, K. P.; Eklund, P. C.; Kostov, M. K.; Cole, M. W. *Phys. Rev. Lett*. **2002**, *88*, 165502.

(23) Field, C. N.; Hamley, P. A.; Webster, J. M.; Gregory, D. H.; Titman, J. J.; Poliakoff, M. *J. Am. Chem. Soc*. **2000**, *2480*, 2480.

(24) Lubezky, A.; Chechelnitsky, L.; Folman, M. *Surf. Sci*. **2000**, *454*, 147.

(25) Folman, M.; Fastow, M.; Kozirovski, Y. *Langmuir* **1997**, *13*, 1118.

(26) Heidberg, J.; Elstner, J.; Lassmann, W.; Folman, M. *J. Electron Spectrosc. Relat. Phenom*. **1993**, *64/65*, 883.

(27) Fastow, M.; Kozirovski, Y.; Folman, M. *J. Electron Spectrosc. Relat. Phenom*. **1993**, *64/65*, 843.

(28) Nagano, Y.; Kiyobayashi, T.; Nitta, T. *Chem. Phys. Lett*. **1994**, *217*, 186.

(29) Mawhinney, D. B.; Rossin, J. A.; Gerhart, K.; Yates, J. T. *Langmuir* **1999**, *15*, 4617.

(30) Kuznetsova, A.; Yates, J. T.; Liu, J.; Smalley, R. E. *J. Chem. Phys*. **2000**, *112*, 9590.

(31) Kuznetsova, A.; Yates, J. T.; Simonyan, V. V.; Johnson, J. K.; Huffman, C. B.; Smalley, R. E. *J. Chem. Phys*. **2001**, *115*, 6691.

(32) Liu, J.; Rinzler, A.; Dai, H.; Hafner, J.; Bradley, R. K.; Boul, P.; Lu, A.; Iverson, T.; Shelimov, K.; Huffman, C. B.; Rodriguez-Macias, F.; Shon, Y.; Lee, T. R.; Colbert, D.; Smalley, R. E. *Science* **1998**, *280*, 1253.

(33) Noda, I. *Appl. Spectrosc*. **1993**, *47*, 1329.

(34) Noda, I. *Appl. Spectrosc*. **2000**, *994*, 994.

(35) Noda, I.; Dowrey, A. E.; Marcott, C.; Story, G. M.; Ozaki, Y. *Appl. Spectrosc*. **2000**, *54*, 236.

(36) Allen, M. P.; Tildesley, D. J. *Computer Simulation of Liquids*; Oxford: Clarendon, 1987.

(37) Harris, J. G.; Yung, K. H. *J. Phys. Chem*. **1995**, *99*, 12021.

(38) Steele, W. A. *Surf. Sci*. **1973**, *36*, 317.

(39) Shi, W.; Johnson, J. K. *Phys. Rev. Lett*. **2003**, *91*, 015504.

(40) Simonyan, V. V.; Johnson, J. K. in preparation.

(41) Shi, W.; Johnson, J. K. in preparation.

(42) Kuznetsova, A.; Popova, I.; Yates, J. T.; Bronikowski, M. J.; Huffman, C. B.; Liu, J.; Smalley, R. E.; Hwu, H. H.; Chen, J. G. *J. Am. Chem. Soc*. **2001**, *123*, 10699.

(43) Yamada, H.; Person, W. B. *J. Chem. Phys*. **1964**, *41*, 2478.

(44) Williams, D. G.; Person, W. B.; Crawford, B. C. *J. Chem. Phys*. **1955**, *23*, 179.

(45) Calbi, M. M.; Cole, M. W. *Phys. Rev. B* **2002**, *66*, 115413.

(46) Calbi, M. M.; Gatica, S. M.; Bojan, M. J.; Cole, M. W. *J. Chem. Phys*. **2001**, *115*,

(47) Gadd, G. E.; Blackford, M.; Moricca, S.; Webb, N.; Evans, P. J.; Smith, A. M.; Jacobsen, G.; Leung, S.; Day, A.; Hua, Q. *Science* **1997**, *277*, 933.